Ongoing Westward Migration of Drainage Divides in Eastern Tibet, Quantified from Topographic Analysis

Chao Zhou[1, 2], Xibin Tan[1, 2, *], Yiduo Liu[3, *], Renqi Lu[1, 2], Michael A. Murphy[3], Honglin He[1, 2], Zhujun Han[1], Xiwei Xu[4]

[1] State Key Laboratory of Earthquake Dynamics, Institute of Geology, China Earthquake Administration, Beijing 100029, China

[2] Shanxi Taiyuan Continental Rift Dynamics National Observation and Research Station, Beijing, 100029, China

[3] Department of Earth and Atmospheric Sciences, University of Houston, Houston, TX 77204-5007, USA

[4] National Institute of Natural Hazards, Beijing, 100085, China

*Corresponding author: tanxibin@ies.ac.cn (X. Tan); yliu54@central.uh.edu (Y. Liu)

Abstract

Landscape evolution is controlled by tectonic strain, bedrock lithology, and climatic conditions, and is expressed in the spatial and temporal variations in river channel networks. In response to tectonic and climatic disturbance, river networks shift both laterally and vertically to achieve a steady state. Several metrics are available to assess the nature of river network disequilibrium, upon which the direction of drainage divide migration can be interpreted. However, to link this information to other observational, theoretical, and experimental data requires the knowledge of the rate of migration, which is still lacking. Here we develop a modified method based on Gilbert metrics to calculate the transient *direction and rate* of drainage divide migration from topography. By choosing a high base level, linear or quasi-linear χ-plots are obtained for rivers on both sides of the drainage divide, and the elevation-χ gradient is proportional to the average normalized steepness index (k_{sn}). In turn, the velocity of divide migration can be quantified theoretically from the cross-divide comparison of χ. We applied this method to eastern Tibet and obtained a uniform, westward migration pattern for 29 points along two drainage divides with rates between 0.02 and 0.66 mm/yr, which is consistent with the great river capture events in the region. The ongoing reorganization of the river network in eastern Tibet is caused by the Cenozoic growth and eastward expansion of the Tibetan Plateau, the strengthening of the precipitation and regional extension throughout East Asia, and the local fault activities.

35 **Keywords:**

36 Divide migration rate; Chi-plot; Channel steepness; Longmen Shan; Eastern Tibet

37

1. Introduction

Landscape evolution is controlled by the development and organization of drainage basins, which is fundamentally controlled by tectonics, lithology, and climatic conditions (Molnar and England, 1990; Whipple, 2009; Zondervan et al., 2020). Geomorphic parameters are widely used to reconstruct past tectonic (e.g., Kirby et al., 2003; Forte et al., 2015; Shi et al., 2021) and climatic processes (e.g., Tucker and Slingerland, 1997; Nie et al., 2018). Tectonic and climate disturbances drive drainage divides to migrate, which impacts river incision by changing the drainage area (Whipple et al., 2017; Vacherat et al., 2018; Yang et al., 2020) and can further influence crustal deformation (Steer et al., 2014; Tan et al., 2018; Liu et al., 2020). Quantitatively measuring the divide migration rate, therefore, is desired as it will not only promote the tectonic and climatic information extraction from topography, but also provide key information for biodiversity conservation (Rahbek et al., 2019).

Drainage divide migration is essentially driven by the cross-divide differential erosion (Willett et al., 2014; Forte and Whipple, 2018; Dahlquist et al., 2018; Hu et al., 2021). Cross-divide erosion rates are routinely derived from geochronological techniques, such as cosmogenic ^{10}Be dating, which have been used to calculate the divide migration rate (Beeson et al., 2017; Hu et al., 2021). Such techniques are usually based on samples collected from the outlet of a few selected drainage basins and may not represent the erosion rates close to the drainage divide as a whole. Ideally, it is necessary to find a cost-effective method that can be applied to the entire

landscape, to cross-check and make full use of the cosmogenic ages. Forte and Whipple (2018) suggested that the cross-divide difference in erosion rate is driven by the cross-divide difference in topographic gradient. The "Gilbert" metrics include the cross-divide difference in channel elevation at a reference drainage area, mean headwater hillslope gradient, and mean headwater local relief and are proposed to judge the stability of drainage divides (Whipple et al., 2017; Forte and Whipple, 2018). However, the erosion rate is affected not only by the topographic gradient, but also by the upstream drainage area, precipitation, and lithology (Howard, 1994; Whipple and Tucker, 1999; Kirby and Whipple, 2012). Therefore, one still cannot obtain the migration rate from the conventional Gilbert metrics. The normalized channel steepness (k_{sn}) is a more reliable and widely-used metric than topographic gradient to reveal erosion rate (Kirby et al., 2001; Wobus et al., 2006; Kirby and Whipple, 2012). In theory, the cross-divide comparison on k_{sn} could be used to quantify the divide migration rate. However, this technique has only been used to judge the direction of drainage divide migration so far (He et al., 2019; Chen et al., 2021).

In this study, we develop a new method modified from the Gilbert metrics to extract the transient divide migration *direction and rate* from topography. We firstly derive an equation for the relationship between the normalized cross-divide differences in erosion rate ($\Delta E/\bar{E}$) and χ ratio (χ_α/χ_β). Then we calculate the top-most χ-plots with high base levels in the eastern Tibetan river network, and obtain the normalized differences in erosion rate based on the equation. We further calculate the

82 divide migration rates based upon the topographic slopes of both sides and the
83 measured or estimated erosion rates. The new formula enables us to map the velocity
84 of drainage divide migration, evaluate the driving mechanisms (Shi et al., 2021), and
85 explores the interactions among various processes in the Earth system (Molnar and
86 England, 1990; Nie et al., 2018).
87

88 ## 2. Method

89 The longitudinal profile of a river records information on bedrock lithology,
90 tectonic strain, and climate history. According to the detachment-limited stream power
91 model (Howard, 1994), the erosion rate, E, is usually expressed in terms of channel
92 gradient, S, and drainage area, A:

93 $$E = KA^m S^n \quad (1)$$

94 or a transformed expression:

95 $$S = \left(\frac{E}{K}\right)^{\frac{1}{n}} A^{\frac{-m}{n}} \quad (2)$$

96 where K is a dimensional coefficient of erosion, and m and n are positive constants
97 that are referred to as area exponent and slope exponent, respectively (Whipple and
98 Tucker, 1999; Kirby and Whipple, 2012). A river longitudinal elevation (z) profile can
99 be expressed by integration in the upstream direction from a base x_b to an observation
100 point x:

101 $$z(x) = z_b + \int_{x_b}^{x} \left(\frac{E(x)}{K(x)}\right)^{\frac{1}{n}} A(x)^{\frac{-m}{n}} dx \quad (3)$$

102 where z_b is the elevation at the river network's base level at $x = x_b$. In the case of

103 spatially invariant erosion rate (E) and erosion coefficient (K), Eq. (3) can be reduced
104 to a simpler form:

105 $$z(x) = z_b + k_{sn}(A_0)^{\frac{-m}{n}}\chi \quad (4)$$

106 with

107 $$k_{sn} = \left(\frac{E}{K}\right)^{\frac{1}{n}} = SA^{\frac{m}{n}} \quad (5)$$

108 and

109 $$\chi = \int_{x_b}^{x}\left(\frac{A_0}{A(x)}\right)^{\frac{m}{n}} dx \quad (6)$$

110 where k_{sn} is the normalized steepness index (Wobus et al., 2006), χ is an integral
111 function of position in the channel network (Perron and Royden, 2013), and A_0 is an
112 arbitrary scaling area, to make the integrand dimensionless. The χ-plot is widely used
113 to analyze the equilibrium of fluvial systems (e.g., Willett et al., 2014; Beeson et al.,
114 2017; Whipple et al., 2017).

115 We rewrite Eqs. (4 & 5):

116 $$E = K \cdot {k_{sn}}^n = K \cdot \left(\frac{z(x)-z_b}{(A_0)^{\frac{-m}{n}}\chi}\right)^n. \quad (7)$$

117 Based on Eq. (7), the normalized difference in erosion rate across the divide is
118 expressed as a function of K, χ, and n:

119 $$\frac{\Delta E}{\bar{E}} = \frac{E_\alpha - E_\beta}{(E_\alpha + E_\beta)/2} = 2 \cdot \frac{K_\alpha/K_\beta - (\chi_\alpha/\chi_\beta)^n}{K_\alpha/K_\beta + (\chi_\alpha/\chi_\beta)^n} \quad (8)$$

120 where E_α is the average erosion rate on the α side, E_β is the average erosion rate on
121 the β side, ΔE is the cross-divide difference in erosion rate ($\Delta E = E_\alpha - E_\beta$), $\bar{E}$ is
122 the average erosion rate across the divide ($\bar{E} = (E_\alpha + E_\beta)/2$), and subscripts α and β
123 denote the two rivers across a divide, assuming that n, A_0, and z_b are uniform across
124 the divide. We plot six curves to illustrate the relationship between the normalized

difference in erosion rate ($\Delta E/\bar{E}$) and χ ratio (χ_α/χ_β) under varying n and K_α/K_β values (Fig. 1). It should be noted that the χ_α and χ_β are not the χ values at a reference area as used by Forte and Whipple (2018), but at a same elevation, in which the reciprocal of χ is proportional to k_{sn}. Also, the assignment of the α and the β side can be arbitrary.

In a simplified scenario, a drainage divide moves a horizontal distance of dx_d over a small time interval dt due to cross-divide difference in elevation change, which, in most cases, is driven by the cross-divide differential erosion (Fig. 2). A simple geometric relationship exists (Beeson et al., 2017; Hu et al., 2021):

$$L_{bd} = L_{ad} - L_{ab} = (E_\alpha - U_\alpha)dt - (E_\beta - U_\beta)dt = (\Delta E - \Delta U)dt \quad (9)$$

and,

$$L_{bd} = L_{bc} + L_{cd} = dx_d(tan\beta + tan\alpha) \quad (10)$$

where L denotes length between two points, t is time, α and β are the slope angles on opposite sides of the divide, U_α is average rock uplift rate on the α side, U_β is average rock uplift rate on the β side, and ΔU is the cross-divide difference in rock uplift rate ($\Delta U = U_\alpha - U_\beta$). Therefore,

$$D_{mr} = \frac{dx_d}{dt} = \frac{\Delta E - \Delta U}{tan\alpha + tan\beta} \quad (11)$$

where D_{mr} is the velocity of drainage divide migration.

From Eq. (8), we can obtain the cross-divide difference in erosion rate, ΔE, when we know K_α/K_β, n, χ_α/χ_β, and the erosion rate around the divide ($\bar{E}$, E_α or E_β). Then, with a known or assumed ΔU, we can calculate the rate of divide migration, D_{mr}, by

147 $$D_{mr} = \frac{\Delta E - \Delta U}{tan\alpha + tan\beta} = \frac{2\bar{E} \cdot \frac{K\alpha/K\beta - (\chi\alpha/\chi\beta)^n}{K\alpha/K\beta + (\chi\alpha/\chi\beta)^n} - \Delta U}{tan\alpha + tan\beta} \quad (12a)$$

148 $$D_{mr} = \frac{E_\alpha \cdot \left[1 - \frac{(\chi\alpha/\chi\beta)^n}{(K\alpha/K\beta)}\right] - \Delta U}{tan\alpha + tan\beta} \quad (12b)$$

149 or

150 $$D_{mr} = \frac{E_\beta \cdot \left[\frac{(K\alpha/K\beta)}{(\chi\alpha/\chi\beta)^n} - 1\right] - \Delta U}{tan\alpha + tan\beta}. \quad (12c)$$

151 The detailed derivation process is shown in Supplementary text.

152 The migration rate can be computed based upon Eq. (12) with the measured or
153 estimated values of E ($\bar{E}$, E_α or E_β), K_α/K_β, χ_α/χ_β, n, ΔU, tanα, and tanβ. The
154 direction of the migration velocity is parallel to the topographic swath profiles and
155 perpendicular to the general trend of the section of the divide.

156

157 # 3. Application in Eastern Tibet

158 ## 3.1 Background, Tools, and Parameters

159 Three major rivers, all tributaries of the Yangtze River, flow out of the eastern
160 Tibetan Plateau. They are, from west to east, the Dadu, Min, and Jialing (including
161 Fu) Rivers. We applied the newly derived method to the Dadu-Min and the Min-
162 Jialing drainage divides (Fig. 3 & 4).

163 To calculate the divide migration rate, we use the Matlab-based toolbox TAK
164 (Forte and Whipple, 2019) and TopoToolbox (Schwanghart and Scherler, 2014) to
165 extract the χ-plot values from ALOS DEM (12.5-m resolution). We obtained the χ-plot
166 with a minimum drainage area of 10^5 m^2 and concavity (m/n) of 0.45 for the drainages

close to major divides in eastern Tibet based on the ALOS DEM (12.5-m resolution). We assigned a high base level (e.g., 3500 m in Fig. 5) to achieve top-most linear or quasi-linear χ-plots. We also assigned the eastern side of the divides as the α side. We then calculated χ_α/χ_β and k_{sn} of each side across the divides. We extract topographic swath profiles to calculate the topographic gradients of both sides of the divide (tanα and tanβ). For error analysis, we used Oracle Crystal Ball software to carry on Monte Carlo simulation for 10^5 times to determine the 1σ deviation of the migration rates, considering the uncertainties in input parameters (E, K_α/K_β, ΔU, tanα, and tanβ).

Rocks in the study area can be grouped into three types based on their erodibility: granitoid, sedimentary rock, and Quaternary sediment (Godard et al., 2010). We chose to analyze the channel pairs in the same rock type with similar precipitation to keep similar erosional coefficients across the divide (i.e., $K_\alpha/K_\beta \approx 1$). In addition, n is another required parameter in Eq. (8). We assumed $n = 1$ in the study area, following previous studies (Kirby and Ouimet, 2011; Kirkpatrick et al., 2020). This assumption is comparable with the ^{10}Be-derived data point from the Longmen Shan on the $\Delta E/\bar{E}$ versus χ_α/χ_β diagram, which is plotted near the $n = 1$ curves (Fig. 1).

Both the Dadu-Min and Min-Jialing divides are at high angles (in strike orientation) to the Longmen Shan thrust belt along the plateau margin and the Longriba fault system to the northwest (Fig. 3c). Although the divides are cut by or close to the Minjiang and Maoergai faults, the selection of high base levels places each channel pair in the same block of the faults. As a result, it is most likely that the

189 difference in rock uplift rate (ΔU) is negligible (0 ± 0.10 mm/yr) within a few
190 kilometers across the two major divides.

191 Several groups have presented lot of ^{10}Be-derived erosion rates in the study area
192 (Fig. 3c). All the elevation of ^{10}Be sample sites are lower than the base level for top-
193 most χ-plots. The ^{10}Be-derived erosion rate, therefore, cover larger area than the top-
194 most χ-plots. Nevertheless, nine ^{10}Be-derived erosion rates (marked as underlined
195 numbers in Fig. 3c) are used as $\bar{E}$, E_α, or E_β for the migration rates calculation at
196 11 divide sites, because they cover relative small area, which has linear or quasi-linear
197 χ-plots (above the knickpoint) (Fig. 6a, c, & d). For the other sites with no selected
198 ^{10}Be data on any side, we assumed an estimated $\bar{E}$ (0.30 ± 0.10 mm/yr). After
199 measuring the topographic gradient of the two sides on the topographic swath profile,
200 we calculated the divide migration rates using Eq. (12), with the measured or
201 estimated erosion rate ($\bar{E}$, E_α, or E_β). And we also calculated the three other
202 parameters in $\bar{E}$, E_α, E_β, and K, according to the topographic parameters and the
203 input independent parameter (Table 1).
204

205 **3.2 Results**

206 We calculated 12 and 17 pairs of χ-plots and topographic gradients (tanα and
207 tanβ) across the Dadu-Min and the Min-Jialing divide, respectively, and obtained the
208 migration direction and rate for each (Fig. 4; Table 1). Details of the results are shown
209 in Fig. 5 and Supplementary Materials (Fig. S1-S10).

210 To examine the influence of the selection of base level, we calculated the χ_α/χ_β

values for a selected profile A-A' in Fig. 5 across the Min-Jialing divide with 31 base levels varying at an interval of 10 m between 3500 m and 3800 m. The result shows that the χ_α/χ_β values are relatively invariant (0.40 ± 0.01) for a base level between 3500 m and 3770 m (Fig. 7), indicating that our calculation is not sensitive to the change of base level, as long as it is high enough. Therefore, we chose a base level of 3500 m to keep a minimal longitudinal length of ~2 km in the four pairs of rivers (Fig. 5). For other river pairs across these two drainage divides, the picked base level elevation ranges from 1700 m to 3950 m (Figs. S2-S9); all are sufficiently high to ensure a stable χ_α/χ_β value.

Our results show that the divide migration velocity at each site has a westward component (Fig. 4; Table 1). The migration rates of the Min-Jialing drainage divide range from 0.02 to 0.66 mm/yr, and those of the Dadu-Min drainage divide range from 0.04 to 0.54 mm/yr. While the majority of the migration rates are less than 0.3 mm/yr on both drainage divides, higher rates are found in the northernmost portions of both divides. On the Min-Jialing divide, the highest three rates (0.46 ± 0.29, 0.66 ± 0.24, 0.38 ± 0.18 mm/yr) fall in the Min Shan fault block between the Minjiang and the Huya fault. On the Dadu-Min divide, the greatest two migration rates (0.38 ± 0.17 and 0.54 ± 0.36 mm/yr) are located near the southwestern tip of the dextral strike-slip Maoergai fault. The highest migration rates are spatially linked to fault zones.

We also plotted the precipitation and the relief within a 500 m radius along four and five segments of the Dadu-Min and the Min-Jialing drainage divide, respectively. The precipitation is indistinguishable across the divide, which supports the

assumption of similar erosional coefficients (i.e., $K_\alpha/K_\beta \approx 1$). The relief on the aggressors' side is either equal to (Figs. S3c, S5c, and S9c) or greater than that on the victims' side (Figs. 5c, S2c, S4c, S6c, S7c, and S8c). Therefore, the overall pattern of the westward divide migration is largely consistent with the cross-divide contrast in relief.

4. Discussion

4.1 Advantage and limitations of the new method

The drainage divide migration is driven by the cross-divide difference in erosion (Willett et al., 2014; Beeson et al., 2017; Whipple et al., 2017; Hu et al., 2021). Willett et al. (2014) proposed the cross-divide difference in χ as a proxy for the basin disequilibrium. Whipple et al. (2017) and Forte and Whipple (2018) proposed the Gilbert metrics to judge the divide stability. We adopted the cross-divide contrast of the χ-plot with a high base level to calculate the velocity of drainage divide migration in this study. Its essence is the cross-divide difference in k_{sn} (Eq. (7)), which could be treated as a Gilbert metric (Whipple et al., 2017; Forte and Whipple, 2018).

The cross-divide difference in k_{sn} is regarded to be effective to judge divide stability but often cannot be measured in the immediate vicinity of the divide (Whipple et al., 2017). Indeed, k_{sn} does not apply to the headwater hillslope region (between the divide and channel head, where the river system initiates). The comparison of erosion rate in this study, therefore, is not immediately across the

254 divide, but a segment just below the channel head (called “channel head segment”
255 hereinafter). The drainage divide migration is directly driven by the differential
256 erosion of the headwater hillslope regions across the divide, mainly via collapse and
257 landslide (Dahlquist et al., 2018). However, under normal circumstances, the erosion
258 rate in the headwater hillslope region on each side can be considered equal to that at
259 the channel head segment. The migration rate in this study, therefore, shall be
260 regarded as an instantaneous rate in most cases. Even if the erosion rate varies from
261 the headwater hillslope region to the channel head segment, the migration rate
262 calculated by our method could be treated as a quasi-instantaneous rate.

263 To further validate our method, we chose a lower base level (800 m) and created
264 the χ-plots for six pairs of rivers in eastern Tibet across the Dadu-Min, the Min-
265 Jialing, and the Anning-Dadu drainage divides (Fig. 6a-f). A crossover appears in the
266 χ-plots of four pairs of the aggressor and victim rivers at an elevation between 1.5 and
267 3.5 km (Fig. 6a-c & f). Rivers 8 and 10 are aggressors, in spite of their relatively high
268 χ value (Fig. 6d & e), which often occur in the case of asymmetric uplift mountain
269 belt (e.g., Fig. 6b in Whipple et al., 2017). Therefore, for a low base level, the cross-
270 divide contrast of channel-head χ values can sometimes fail to reflect the
271 instantaneous migration of drainage divide (Fig. 6a-f).

272 We suggest that the stability of the drainage divide is only controlled by the
273 gradient at the top of the elevation-χ curve. We use three diagrams to illustrate this
274 argument (Fig. 6g-i). When a disturbance, such as asymmetric uplift, occurs, the
275 drainage system loses its stability, and the divide begins to migrate (Fig. 6g). The

aggressor river has a higher χ than the victim river if a low base level at z_{b1} is used (Fig. 6h). In contrast, for a high base level at z_{b2}, the aggressor river yields a lower χ than the victim river (Fig. 6i). One can identify the aggressor and the victim rivers correctly only in the latter case. This highlights the necessity of choosing a high base level in the χ-plot method for the analysis of drainage divide migration.

All methods that judge drainage divide stability, including ours, could be disturbed by variations in erosion coefficient (K, including lithology and precipitation) or asymmetric uplift (Forte and Whipple, 2018; He et al., 2019; Shi et al., 2021). For instance, (1) different K may cause different headwater hillslope gradient and different channel elevation at a reference drainage area across the divide, even if the drainage divide is actually in equilibrium; (2) the divide migration rate in this study could be underestimated or overestimated in the situation of an east- or westward tilt, respectively. Therefore, we chose the sites with similar lithology, precipitation, and uplift rate across the divide when comparing the cross-divide differences in each geomorphic parameter to judge the divide stability. Nevertheless, if the spatial variations in erosion coefficient (K) and uplift rate (U) are known, one can quantitatively assess their influences on the migration of the drainage divide, according to Eq. (12).

The erosion rate, E ($\bar{E}$, E_α, or E_β), is usually unknown, which is a major limitation of this method. If the exact K values are constrained, one can calculate the erosion rate of each side (E_α and E_β) from k_{sn} and K values (Eq. (7); Kirby et al., 2001; Duvall et al., 2004; DiBiase et al., 2018; Ma et al., 2020), and then the

298 migration rate can be obtained by Eq. (11). In principle, one of these four parameters
299 on erosion ($\bar{E}$, E_α, E_β, or K, measured by ^{10}Be or other independent methods) is
300 required in the calculation of divide migration rate, and the rest three parameters can
301 be calculated from the topographic parameters (k_{sn} and χ) (Table 1). If all the four
302 parameters on erosion are unknown, one could use an estimated $\bar{E}$ or K, based on the
303 regional average erosion rate derived from ^{10}Be and other methods (Fig. 3c; Table 1).
304 In this case, using an estimated $\bar{E}$ is preferred, because the K value, affected by the
305 lithology, precipitation, and distance to the active fault, usually has a large variation
306 (Kirkpatrick et al., 2020; Zondervan et al., 2020), whereas the $\bar{E}$ value is relatively
307 less variable.

308 In general, the migration rate calculation needs parameters of E ($\bar{E}$, E_α or E_β),
309 K_α/K_β, χ_α/χ_β, n, ΔU, tanα, and tanβ. Among these parameters, χ_α/χ_β, tanα, and
310 tanβ are derived from DEM, which have few errors. The others (E, K_α/K_β, n, and
311 ΔU) are inputted parameters based on the actual situation or other independent
312 methods, which may bring uncertainties to the divide migration rate. Although the
313 calculation of divide migration rate in this study may have great uncertainty (Table 1;
314 Fig. S10), we can acquire more accurate divide migration rates with the improvement
315 of accuracy on these inputted parameters.
316
317 **4.2 Drainage evolution in eastern Tibet and its tectonic implications**
318 A drainage divide in a symmetrical mountain tends to migrate to the side with a
319 greater uplift rate or lower erosion coefficient (stronger lithology or lower

320 precipitation) (Goren et al., 2014; Shi et al., 2021). Figure 8 shows conceptually how
321 disturbance by tectonic strain, lithology, and climate, respectively, can cause the
322 drainage divide migration.

323 In the eastern Tibetan Plateau, great rivers mainly flowed southeastward during
324 the early Cenozoic (Clark et al., 2004). Following the Cenozoic India-Asia collision,
325 surface uplift of the Tibetan Plateau changed the regional slope trend, causing a
326 reorganization of the drainage system in eastern Tibet (Clark et al., 2004; Zhang et al.,
327 2014; Yang et al., 2020). All Cenozoic great capture events in eastern Tibet show a
328 pattern of which the drainage on the east invaded the one on the west (Fig. 3a). Our
329 results reveal that the Dadu-Min and the Min-Jialing drainage divides both migrated
330 westward at present, which is spatially consistent with the general trend of the great
331 capture events in geological history. Moreover, our results are consistent with
332 previous research on thermochronology and cosmogenic ^{10}Be dating, which suggested
333 the westward regressive erosion in response to a pulse of uplift (since ~10 Ma) along
334 the eastern margin of the Tibetan Plateau (Godard et al., 2010; Tian et al., 2015;
335 Ansberque et al., 2015, 2018; Wang et al., 2021).

336 The westward migration of the drainage divides in the eastern Tibetan Plateau is
337 a response to the tectonic, climatic, and lithological disturbance at both the regional
338 and the local scales. The tectonic disturbance is reflected by both surface exhumation
339 and crustal deformation in the study area (Fig. 9). Except for some young ages in the
340 hanging-wall of the reverse faults (e.g., the Wenchuan and the Huya Faults), the
341 apatite fission track ages show generally an increasing trend from west to east,

indicating a decreasing trend of uplift rate from west to east in the study area (Fig. 9a). Such an increasing trend of ages is not caused by the variation in the samples' elevation; for instance, samples in the Jialing drainage were collected from the lowest elevations (Figs. 9c & S12). The spatial difference in uplift is also recorded by the χ-plots of the channels with a lower base level (Fig. 6) and the k_{sn} map (Fig. 9a), both of which show all victim drainages have higher k_{sn} in the downstream area than the aggressor drainages do.

Cenozoic thickening and growth of the eastern Tibetan Plateau is associated with both brittle deformation in the upper crust, as demonstrated by thrusts and strike-slip faults and their related folds, and viscous, partially-molten rocks in the mid-to-lower crust, as characterized by the high conductivity, low velocity, seismically anisotropic anomalies under the interior of the plateau (Clark and Royden, 2000; Bai et al., 2010; Bao et al., 2020; Liu et al., 2021). The Moho shallows eastward from nearly 60 km depth under the interior of the Tibetan Plateau to almost 40 km in the Sichuan Basin (Wei et al., 2017; Xu et al., 2018; Tan et al., 2019; Lu et al., 2019). At a finer scale, the Moho is offset by a set of reverse faults (Fig. 9b&d) (Guo et al., 2013). Tan et al. (2019) suggested that the eastward motion of the Tibetan crust drives both thrust faulting in the upper crust and ductile shearing and thickening in the mid-to-lower crust. Crustal deformation in this area, therefore, can cause a gentle, east-dipping tilt on the surface (Fig. 9d). Also, the Cenozoic India-Asia collision and the Pacific subduction and trench retreat have driven widespread crustal extension and subsidence throughout East Asia (Northrup et al., 1995; Yin, 2010; Su et al., 2021),

364 which facilitated the formation and connection of large rivers from the Tibetan
365 Plateau to the East Asian marginal seas (e.g., Clark et al., 2004; Zheng et al., 2013).
366 Moreover, the Cenozoic uplift and growth of the Tibetan Plateau has influenced
367 the East Asian monsoon and strengthened the precipitation in East Asia (Farnsworth et
368 al., 2021). The precipitation rate decreases from more than 1000 mm/yr in the Sichuan
369 basin to ~700 mm/yr in the interior of eastern Tibet (Fig. 3b). All these processes can
370 further intensify the westward divide migration in eastern Tibet (Fig. 9).
371 Besides the large-scale tectonic and climatic disturbance in eastern Tibet, local
372 fault activities must have also impacted the drainage reorganization (Ansberque et al.,
373 2015; Yang et al., 2020) by changing (most likely enhancing) the rock erodibility
374 (Kirkpatrick et al., 2020) (Fig. 8b). Ansberque et al. (2015) suggested the activity of
375 the Maoergai fault caused the northwestward expending of the Min drainage basin.
376 Our study reveals that the migration rates of the Dadu-Min divide close to the
377 Maoergai fault are noticeably higher than others on the same divide, implying the
378 localized influence of the Maoergai fault activity on the divide migration. Similarly,
379 the relatively high migration rates on the northern half of the Min-Jialing divide could
380 also be attributed to the activity of the Huya fault (Fig. 4).
381 In brief, our analysis on the stability of drainage divides in the eastern Tibetan
382 Plateau demonstrates that the drainage systems here are not in equilibrium, and the
383 westward migration of drainage divides is still ongoing. The westward drainage
384 divide migration could be driven by the Cenozoic uplift and growth of the Tibetan
385 Plateau, regional extension and subsidence throughout East Asia, strengthening of

386 precipitation, and local fault activities. How to quantitatively differentiate these
387 factors, however, is beyond the scope of this study, but deserves rigorous analysis in
388 future studies.
389

390 ## 5. Conclusions

391 (1) We have developed a new theoretical relationship between the normalized
392 difference in erosion rate and χ ratio (Eq. (8); Fig. 1). It permits quantification of the
393 velocity (i.e., direction and magnitude) of drainage divide migration from topography.
394 We developed a new workflow to achieve the calculation, based on existing software,
395 including the Matlab-based TAK and TopoToolbox, ArcMap GIS platform, and
396 Oracle Crystal Ball, and publically available ALOS DEM data.
397 (2) We applied this new method to the drainage systems in eastern Tibet and
398 obtained 29 transient divide migration velocities on the Dadu-Min and the Min-Jialing
399 drainage divides. All drainage divides are migrating westward, and their rates vary
400 between 0.02 and 0.66 mm/yr on the Min-Jialing drainage divide and between 0.04
401 and 0.54 mm/yr for the Dadu-Min drainage divide.
402 (3) Our findings are consistent with the past great capture events in the eastern
403 Tibetan Plateau. The drainage systems in eastern Tibet are not in equilibrium, and the
404 westward migration of drainage divides is still ongoing, driven by multiple factors at
405 the regional and local scales.
406

Declaration of Competing Interest

The authors declare that they have no known competing financial interests or personal relationships that could have influenced this work.

Acknowledgments

This study is supported by the Fundamental Research Funds from the Institute of Geology, China Earthquake Administration (IGCEA2004). YL thanks the Governor's University Research Initiative (GURI) Fund from the State of Texas and the University of Houston awarded to Prof. John Suppe. We thank Drs. Sean Willett, Zhanyu Wei, Feng Shi, and Suoya Fan for helpful suggestions which improved the manuscript. The topography data is from https://search.asf.alaska.edu/. The precipitation data are downloaded from http://worldclim.org. The indices in this paper are calculated through TAK (Forte and Whipple, 2019) and TopoToolbox (Schwanghart and Scherler, 2014) on MATLAB.

References

Ansberque, C., Godard, V., Bellier, O., De Sigoyer, J., Liu-Zeng, J., Xu, X., Ren, Z., Li, Y., Team, A.S.T.E.R., 2015. Denudation pattern across the Longriba fault system and implications for the geomorphological evolution of the eastern Tibetan margin. Geomorphology 246, 542-557. https://doi.org/10.1016/j.geomorph.2015.07.017

Ansberque, C., Godard, V., Bellier, O., de Sigoyer, J., Bernet, M., Stubner, K., Tan, X., Xu, X., Ehlers, T.A., 2018. Differential Exhumation Across the Longriba Fault System: Implications for the Eastern Tibetan Plateau. Tectonics 37,

2017TC004816. http://doi.org/10.1002/2017TC004816
Beeson, H.W., McCoy, S.W., Keen-Zebert, A., 2017. Geometric disequilibrium of river basins produces long-lived transient landscapes. Earth Planet. Sci. Lett. 475, 34-43. https://doi.org/10.1016/j.epsl.2017.07.010
Bai, D., Unsworth, M.J., Meju, M.A., Ma, X., Teng, J., Kong, X., Sun, Y., Sun, J., Wang, L., Jiang, C., Zhao, C., 2010. Crustal deformation of the eastern Tibetan plateau revealed by magnetotelluric imaging. Nat. Geosci. 3(5), 358-362. https://doi.org/10.1038/ngeo830
Bao, X., Song, X., Eaton, D.W., Xu, Y., Chen, H., 2020. Episodic lithospheric deformation in eastern Tibet inferred from seismic anisotropy. Geophys. Res. Lett. 47(3), e2019GL085721. https://doi.org/10.1029/2019GL085721
Clark, M.K., Royden, L.H., 2000. Topographic ooze: Building the eastern margin of Tibet by lower crustal flow. Geology 28(8), 703-706. https://doi.org/10.1130/0091-7613(2000)28<703:TOBTEM>2.0.CO;2
Clark, M.K., Schoenbohm, L.M., Royden, L.H., Whipple, K.X., Burchfiel, B.C., Zhang, X., Tang, W., Wang, E., Chen, L., 2004. Surface uplift, tectonics, and erosion of eastern Tibet from large-scale drainage patterns. Tectonics 23, 1-20. https://doi.org/10.1029/2002TC001402
Clark, M.K., House, M.A., Royden, L.H., Whipple, K.X., Burchfiel, B.C., Zhang, X., Tang, W., 2005. Late Cenozoic uplift of southeastern Tibet. Geology 33 (6), 525-528. https://doi.org/10.1130/G21265.1
Dahlquist, M.P., West, A.J., and Li, G., 2018. Landslide-driven drainage divide migration. Geology, https://doi.org/10.1130/G39916.1
DiBiase, R.A., Rossi, M.W. and Neely, A.B., 2018. Fracture density and grain size controls on the relief structure of bedrock landscapes. Geology, 46(5), 399-402. https://doi.org/10.1130/G40006.1
Duvall, A., Kirby, E. and Burbank, D., 2004. Tectonic and lithologic controls on bedrock channel profiles and processes in coastal California. Journal of Geophysical Research: Earth Surface, 109(F3). https://doi.org/10.1029/2003JF000086
Enkelmann, E., Ratschbacher, L., Jonckheere, R., Nestler, R., Fleischer, M., Gloaguen, R., Hacker, B.R., Zhang, Y.Q. and Ma, Y.S., 2006. Cenozoic exhumation and deformation of northeastern Tibet and the Qinling: Is Tibetan lower crustal flow diverging around the Sichuan Basin? Geol. Soc. Am. Bull. 118 (5-6), 651-671. https://doi.org/10.1130/B25805.1
Farnsworth, A., Lunt, D.J., Robinson, S.A., Valdes, P.J., Roberts, W.H., Clift, P.D., Markwick, P., Su, T., Wrobel, N., Bragg, F. and Kelland, S.J., 2019. Past East Asian monsoon evolution controlled by paleogeography, not CO_2. Science Advances, 5(10), p.eaax1697. https://doi.org/10.1126/sciadv.aax1697
Forte, A.M., Whipple, K.X. and Cowgill, E., 2015. Drainage network reveals patterns and history of active deformation in the eastern Greater Caucasus. Geosphere, 11(5), 1343-1364. https://doi.org/10.1130/GES01121.1
Forte, A.M., Whipple, K.X., 2018. Criteria and tools for determining drainage divide stability. Earth Planet. Sci. Lett. 493, 102–117.

https://doi.org/10.1016/j.epsl.2018.04.026
Forte, A.M., Whipple, K.X., 2019. Short communication: The Topographic Analysis Kit (TAK) for TopoToolbox. Earth Surface Dynamics 7, 87–95. https://doi.org/10.5194/esurf-7-87-2019
Godard, V., Lavé, J., Carcaillet, J., Cattin, R., Bourlès, D., Zhu, J., 2010. Spatial distribution of denudation in Eastern Tibet and regressive erosion of plateau margins. Tectonophysics 491(1-4), 253-274. https://doi.org/10.1016/j.tecto.2009.10.026
Goren, L., Willett, S. D., Herman, F., Braun, J., 2014. Coupled numerical–analytical approach to landscape evolution modeling. Earth Surface Processes and Landforms, 39(4), 522-545. https://doi.org/10.1002/esp.3514
Guo, X., Gao, R., Keller, G.R., Xu, X., Wang, H., Li, W., 2013. Imaging the crustal structure beneath the eastern Tibetan Plateau and implications for the uplift of the Longmen Shan range. Earth Planet. Sci. Lett. 379, 72-80. https://doi.org/10.1016/j.epsl.2013.08.005
He, C., Rao, G., Yang, R., Hu, J., Yao, Q., Yang, C.J., 2019. Divide migration in response to asymmetric uplift: Insights from the Wula Shan horst, North China. Geomorphology, 339, 44-57. https://doi.org/10.1016/j.geomorph.2019.04.024
Howard, A.D., 1994, A detachment-limited model of drainage basin evolution: Water Resources Research, 30, 2261–2285. https://doi.org/10.1029/94WR00757
Hu, K., Fang, X., Ferrier, K.L., Granger, D.E., Zhao, Z., Ruetenik, G.A., 2021. Covariation of cross-divide differences in denudation rate and χ: Implications for drainage basin reorganization in the Qilian Shan, northeast Tibet. Earth Planet. Sci. Lett. 562, 116812. https://doi.org/10.1016/j.epsl.2021.116812
Kirby, E., Ouimet, W., 2011. Tectonic geomorphology along the eastern margin of Tibet: Insights into the pattern and processes of active deformation adjacent to the Sichuan Basin. Geol. Soc. London Sp. Pub. 353(1), 165-188. https://doi.org/10.1144/SP353.9
Kirby, E., Whipple, K., 2001. Quantifying differential rock-uplift rates via stream profile analysis. Geology 29(5), 415-418. https://doi.org/10.1130/0091-7613(2001)029<0415:QDRURV>2.0.CO;2
Kirby, E., Whipple, K.X., 2012. Expression of active tectonics in erosional landscapes. J. Struct. Geol. 44, 54-75. https://doi.org/10.1016/j.jsg.2012.07.009
Kirby, E., Whipple, K.X., Tang, W., Chen, Z., 2003. Distribution of active rock uplift along the eastern margin of the Tibetan Plateau: Inferences from bedrock channel longitudinal profiles. J. Geophys. Res.: Solid Earth 108(B4), 1-16. https://doi.org/10.1029/2001JB000861
Kirkpatrick, H.M., Moon, S., Yin, A., Harrison, T.M., 2020. Impact of fault damage on eastern Tibet topography. Geology 49, 30-34. https://doi.org/10.1130/G48179.1
Liang, S., Gan, W., Shen, C., Xiao, G., Liu, J., Chen, W., Ding, X., Zhou, D., 2013. Three- dimensional velocity field of present- day crustal motion of the Tibetan Plateau derived from GPS measurements. J. Geophys. Res.: Solid Earth 118(10),

5722-5732. https://doi.org/10.1002/2013JB010503
Liu, Y., Tan, X., Ye, Y., Zhou, C., Lu, R., Murphy, M.A., Xu, X., Suppe, J., 2020. Role of erosion in creating thrust recesses in a critical-taper wedge: An example from Eastern Tibet. Earth Planet. Sci. Lett. 540, 116270. https://doi.org/10.1016/j.epsl.2020.116270
Liu, Y., Li, L., van Wijk, J.W., Li, A., Fu, Y.V., 2021. Surface wave tomography of the Emeishan large igneous province: Magma storage system, hidden hotspot track, and its impact on the Capitanian mass extinction. Geology. https://doi.org/10.1130/G49055.1
Lu, R., Liu, Y., Xu, X., Tan, X., He, D., Yu, G., Cai, M., and Wu, X., 2019. Three-dimensional model of the lithospheric structure under the eastern Tibetan Plateau: Implications for the active tectonics and seismic hazards. Tectonics 38(4), 1292-1307. https://doi.org/10.1029/2018TC005239
Ma, Z., Zhang, H., Wang, Y., Tao, Y. and Li, X., 2020. Inversion of Dadu River bedrock channels for the late cenozoic uplift history of the eastern Tibetan Plateau. Geophysical Research Letters, 47(4), p.e2019GL086882. https://doi.org/10.1029/2019GL086882
Molnar, P., England, P., 1990. Late Cenozoic uplift of mountain ranges and global climate change: chicken or egg? Nature 346(6279), 29-34. https://doi.org/10.1038/346029a0
Nie, J., Ruetenik, G., Gallagher, K., Hoke, G., Garzione, C.N., Wang, W., Stockli, D., Hu, X., Wang, Z., Wang, Y. and Stevens, T., 2018, Rapid incision of the Mekong River in the middle Miocene linked to monsoonal precipitation: Nature Geoscience, 11(12), 944-948. https://doi.org/10.1038/s41561-018-0244-z
Northrup, C.J., Royden, L.H. and Burchfiel, B.C., 1995. Motion of the Pacific plate relative to Eurasia and its potential relation to Cenozoic extension along the eastern margin of Eurasia. Geology, 23(8), 719-722. https://doi.org/10.1130/0091-7613(1995)023<0719:MOTPPR>2.3.CO;2
Perron, J.T., Royden, L., 2013. An integral approach to bedrock river profile analysis. Earth Surface Processes and Landforms 38(6), 570-576. http://dx.doi.org/10.1002/esp.3302
Rahbek, C., Borregaard, M.K., Antonelli, A., Colwell, R.K., Holt, B.G., Nogues-Bravo, D., Rasmussen, C.M., Richardson, K., Rosing, M.T., Whittaker, R.J. and Fjeldså, J., 2019. Building mountain biodiversity: Geological and evolutionary processes. Science, 365(6458), 1114-1119. https://www.doi.org/10.1126/science.aax0151
Scherler, D., Schwanghart, W., 2020. Drainage divide networks – Part 2: Response to perturbations. Earth Surface Dynamics 8(2), 261-274. https://doi.org/10.5194/esurf-8-261-2020
Schwanghart, W., Scherler, D., 2014. Short Communication: TopoToolbox 2 – MATLAB-based software for topographic analysis and modeling in Earth surface sciences. Earth Surface Dynamics 2 (1), 1-7. https://doi.org/10.5194/esurf-2-1-2014
Shi, F., Tan, X., Zhou, C., Liu, Y., 2021. Impact of asymmetric uplift on mountain

562 asymmetry: Analytical solution, numerical modeling, and natural examples.
563 Geomorphology, 107862. https://doi.org/10.1016/j.geomorph.2021.107862
564 Steer, P., Simoes, M., Cattin, R., Shyu, J.B.H., 2014. Erosion influences the seismicity
565 of active thrust faults. Nature Communications, 5, 5564.
566 https://doi.org/10.1038/ncomms6564
567 Su, P., He, H., Tan, X., Liu, Y., Shi, F., Kirby, E., 2021. Initiation and evolution of the
568 Shanxi Rift System in North China: Evidence from low- temperature
569 thermochronology in a plate reconstruction framework. Tectonics,
570 e2020TC006298. https://doi.org/10.1029/2020TC006298
571 Tan, X.B., Lee, Y.H., Chen, W.Y., Cook, K.L., Xu, X.W., 2014. Exhumation history
572 and faulting activity of the southern segment of the Longmen Shan, eastern
573 Tibet. J. Asian Earth Sci. 81, 91-104. https://doi.org/10.1016/j.jseaes.2013.12.002
574 Tan, X.B., Lee, Y. H., Xu, X.W., Cook, K.L., 2017a. Cenozoic exhumation of the
575 Danba antiform, eastern Tibet: Evidence from low-temperature
576 thermochronology. Lithosphere 9(4), 534-544. https://doi.org/10.1130/L613.1
577 Tan, X.B., Xu, X.W., Lee, Y.H., Lu, R.Q., Liu, Y., Xu, C., Li, K., Yu, G.H., Kang,
578 W.J., 2017b. Late Cenozoic thrusting of major faults along the central segment of
579 Longmen Shan, eastern Tibet: Evidence from low-temperature
580 thermochronology. Tectonophysics 712, 145-155.
581 https://doi.org/10.1016/j.tecto.2017.05.016
582 Tan, X., Yue, H., Liu, Y., Xu, X., Shi, F., Xu, C., Ren, Z., Shyu, J.B.H., Lu, R. and
583 Hao, H., 2018. Topographic loads modified by fluvial incision impact fault
584 activity in the Longmenshan thrust belt, eastern margin of the Tibetan Plateau.
585 Tectonics 37(9), 3001-3017. https://doi.org/10.1029/2017TC004864
586 Tan, X., Liu, Y., Lee, Y.H., Lu, R., Xu, X., Suppe, J., Shi, F., Xu, C., 2019. Parallelism
587 between the maximum exhumation belt and the Moho ramp along the eastern
588 Tibetan Plateau margin: Coincidence or consequence?. Earth Planet. Sci. Lett.
589 507, 73-84. https://doi.org/10.1016/j.epsl.2018.12.001
590 Tian, Y., Kohn, B.P., Hu, S., Gleadow, A.J., 2015. Synchronous fluvial response to
591 surface uplift in the eastern Tibetan Plateau: Implications for crustal dynamics.
592 Geophys. Res. Lett. 42(1), 29-35. https://doi.org/10.1002/2014GL062383
593 Tian, Y., Li, R., Tang, Y., Xu, X., Wang, Y., Zhang, P., 2018. Thermochronological
594 constraints on the late Cenozoic morphotectonic evolution of the Min Shan, the
595 eastern margin of the Tibetan Plateau. Tectonics 37(6), 1733-1749.
596 https://doi.org/10.1029/2017TC004868
597 Tucker, G.E., Slingerland, R., 1997. Drainage basin responses to climate change.
598 Water Resources Research, 33 (8), 2031-2047.
599 https://doi.org/10.1029/97WR00409
600 Vacherat, A., Bonnet, S., Mouthereau, F., 2018. Drainage reorganization and divide
601 migration induced by the excavation of the Ebro basin (NE Spain). Earth Surface
602 Dynamics 6 (2), 369-387. https://doi.org/10.5194/esurf-6-369-2018
603 Wang, E., Kirby, E., Furlong, K.P., Van Soest, M., Xu, G., Shi, X., Kamp, P.J.,
604 Hodges, K.V., 2012. Two-phase growth of high topography in eastern Tibet
605 during the Cenozoic. Nat. Geosci. 5(9), 640-645.

https://doi.org/10.1038/ngeo1538
Wang, W., Godard, V., Liu- Zeng, J., Zhang, J., Li, Z., Xu, S., Yao, W., Yuan, Z., Aumaître, G., Bourlès, D.L., and Keddadouche, K., 2021. Tectonic controls on surface erosion rates in the Longmen Shan, Eastern Tibet. Tectonics, e2020TC006445. https://doi.org/10.1029/2020TC006445
Wei, X., Jiang, M., Liang, X., Chen, L., Ai, Y., 2017. Limited southward underthrusting of the Asian lithosphere and material extrusion beneath the northeastern margin of Tibet, inferred from teleseismic Rayleigh wave tomography. J. Geophys. Res.: Solid Earth, 122, 7172-7189. https://doi.org/10.1002/2016JB013832
Whipple, K.X., Tucker, G.E., 1999. Dynamics of the stream-power river incision model: Implications for height limits of mountain ranges, landscape response timescales, and research needs. J. Geophys. Res., Solid Earth 104 (B8), 17661-17674. https://doi.org/10.1029/1999JB900120
Whipple, K.X., 2009. The influence of climate on the tectonic evolution of mountain belts. Nat. Geosci. 2 (2), 97-104. https://doi.org/10.1038/ngeo413
Whipple, K.X., Forte, A.M., DiBiase, R.A., Gasparini, N.M., Ouimet, W.B., 2017. Timescales of landscape response to divide migration and drainage capture: Implications for the role of divide mobility in landscape evolution. J. Geophys. Res., Earth Surface, 122 (1), 248-273. https://doi.org/10.1002/2016JF003973
Willett, S.D., McCoy, S.W., Perron, J.T., Goren, L., Chen, C.Y., 2014. Dynamic reorganization of river basins. Science 343 (6175), 1117. https://doi.org/10.1126/science.1248765
Wilson, C.J., Fowler, A.P., 2011. Denudational response to surface uplift in east Tibet: Evidence from apatite fission-track thermochronology. Geological Society of America Bulletin 123 (9-10), 1966-1987. https://doi.org/10.1130/B30331.1
Wobus, C., Whipple, K.X., Kirby, E., Snyder, N., Johnson, J., Spyropolou, K., Crosby, B., Sheehan, D., 2006. Tectonics from topography: Procedures, promise, and pitfalls. Geological Society of America Special Papers 398, 55-74. https://doi.org/10.1130/2006.2398(04)
Yang, R., Suhail, H.A., Gourbet, L., Willett, S.D., Fellin, M.G., Lin, X., Gong, J., Wei, X., Maden, C., Jiao, R., Chen, H., 2020. Early Pleistocene drainage pattern changes in Eastern Tibet: Constraints from provenance analysis, thermochronometry, and numerical modeling. Earth Planet. Sci. Lett. 531, 1-10. https://doi.org/10.1073/pnas.1216241110
Yin, A., 2010. Cenozoic tectonic evolution of Asia: A preliminary synthesis. Tectonophysics 488(1-4), 293-325. https://doi.org/10.1016/j.tecto.2009.06.002
Xu, G., Kamp, P.J., 2000. Tectonics and denudation adjacent to the Xianshuihe Fault, eastern Tibetan Plateau: Constraints from fission track thermochronology. J. Geophys. Res., Solid Earth 105 (B8), 19231-19251. https://doi.org/10.1029/2000JB900159
Xu, X., Niu, F., Ding, Z., Chen, Q., 2018. Complicated crustal deformation beneath the NE margin of the Tibetan Plateau and its adjacent areas revealed by multi-station receiver-function gathering. Earth and Planetary Science Letters, 497,

204-216. https://doi.org/10.1016/j.epsl.2018.06.010
Zhang, H., Zhang, P., Champagnac, J.D., Molnar, P., Anderson, R.S., Kirby, E., Craddock, W.H., Liu, S., 2014. Pleistocene drainage reorganization driven by the isostatic response to deep incision into the northeastern Tibetan Plateau. Geology 42 (4), 303-306. https://doi.org/10.1130/G35115.1
Zheng, H., Clift, P.D., Wang, P., Tada, R., Jia, J., He, M., Jourdan, F., 2013. Pre-Miocene birth of the Yangtze River. Proceedings of the National Academy of Sciences 110 (19), 1-6. https://doi.org/10.1073/pnas.1216241110
Zondervan, J.R., Stokes, M., Boulton, S.J., Telfer, M.W., Mather, A.E., 2020. Rock strength and structural controls on fluvial erodibility: Implications for drainage divide mobility in a collisional mountain belt. Earth and Planetary Science Letters 538, 116221. https://doi.org/10.1016/j.epsl.2020.116221

Figure captions

Figure 1. Quantitative relationship between normalized difference in erosion rate and χ ratio across a drainage divide, based on Eq. (8). The relationship is a function of the cross-divide ratio of erosional coefficient (K_α/K_β) and slope exponent (n). Data sources: Ozark Dome from Beeson et al. (2017), Eastern Tibet from Ansberque et al. (2015) and Kirkpatrick et al. (2020).

Figure 2. Schematic illustration in cross-section view for drainage divide migration. The two triangles represent the cross-divide river longitudinal profiles before (dashed) and after (solid) an infinitesimal interval of time (dt). α and β are slopes across the divide; when in subscript, they denote the two rivers across the divide. E is erosion rate, and U is rock uplift rate. dx_d is the horizontal distance of the drainage divide migration, which is the product of drainage divide migration velocity (D_{mr}) and dt. Lowercase letters a-d mark the four points on the auxiliary lines (dotted).

Figure 3. (a) Major drainage systems and the great Cenozoic capture events in the eastern and southeastern Tibetan Plateau. (b) Precipitation distribution in the same region. Precipitation data (1970-2000) are from http://worldclim.org. Inset is a plot of precipitation along a 60-km-wide swath profile P-P'. Black curve indicates the mean precipitation and the grey shade below the curve shows the maximum and minimum

684 precipitation. (c) Map of published cosmogenic ^{10}Be ages and the derived erosion
685 rates. The underlined numbers and non-transparent coloring indicate the erosion rates
686 and their covering areas that are applied directly in the calculation of divide
687 migration. Others are only applied for the estimation of regional average erosion rate.
688 Data sources: Ouimet et al. (2009), Godard et al. (2010), Ansberque et al. (2015), and
689 Kirkpatrick et al. (2020).
690
691 **Figure 4.** Drainage system in eastern Tibet and the calculated migration velocity of
692 the Dadu-Min and Min-Jialing divides. Dark blue vector indicates the velocity of
693 drainage divide migration. See Table 1 for direction and magnitude. Red curve marks
694 the drainage divide. Thick, translucent curves indicate the channels 1-10 in Fig. 7,
695 whose base level elevations are 800 m.
696
697 **Figure 5.** (a) χ map of a upstream region of the Min and Jialing river drainages, with a
698 uniform base elevation at 3500 m. See Fig. 4 for location. (b) χ-plots for four pairs of
699 rivers across the Min-Jialing drainage divide (left) and their swath profiles of
700 topography (right) along A-A', B-B', C-C', and D-D'. Numbers in the χ-plots are the χ
701 values at the same top-most elevation and the average k_{sn} values (the underlined
702 numbers) in units of $m^{0.9}$. Numbers with no unit in the right panel are the values of
703 tanα and tanβ. The velocity of divide migration is labelled on top of the divide. The K
704 value of each site is in units of $10^{-6}m^{0.1}yr^{-1}$. (c) Precipitation (http://worldclim.org)
705 and relief (within 500 m radius) along the drainage divide E-E' (see Fig. 5a for

706 location). The swath profiles E-E' extends to both sides of the drainage divide by 2
707 km and 0.5 km for precipitation and relief, respectively.
708
709
710 **Figure 6.** (a-f) Comparison of χ-plots of six pairs of rivers with a base elevation of
711 800 m. The locations of channels 1-10 are shown in Fig. 4. Channels 11 and 12 are
712 two rivers in the southeastern Tibet from Yang et al. (2020) and their locations are not
713 shown in this study. Note that: (1) In each diagram, the victim river shows a greater
714 slope of elevation-χ (i.e., higher k_{sn}) than the aggressor river does in the downstream
715 area; in contrast, the victim river has a smaller slope of elevation-χ (i.e., lower k_{sn}) in
716 the upstream area (above the marked knickpoints). (2) Channels 7 and 9 are victims,
717 although they have lower χ values for the full basin than channels 8 and 10 do,
718 respectively. (3) The elevations of base level for the top-most χ-plots, the knickpoints,
719 and four ^{10}Be samples are presented. The elevations of other ^{10}Be samples are shown
720 in Figure S11. (g-i) Schematic diagrams of disequilibrium of drainage systems in
721 response to asymmetric uplift, and its χ-plot with different base levels (z_{b1} and z_{b2}).
722
723 **Figure 7.** A test on the selection and stability of base levels. (a) Varying base level z_b
724 versus its corresponding χ_α/χ_β values. The base level increases from 3500 m to
725 3800 m at an increment of 10 m. The χ_α/χ_β values fall around 0.4 for base levels

between 3500 and 3770 m. (b) Histogram and frequency distribution of the calculated χ_α/χ_β values for varying base level elevations.

Figure 8. Cartoon diagrams for drainage divide migration caused by tectonic (a), lithological (b), and climatic (c) disturbances, respectively. It should be noted that the divide is in equilibrium before these disturbances, and the diagrams show the initial status after each disturbance.

Figure 9. (a) Topography, normalized channel steepness, major faults, and apatite fission track ages in eastern Tibet. Thick red curves denote the Dadu-Min and the Min-Jialing drainage divides, and black are major faults. Yellow stars show the location and ages of the published apatite fission track samples. References: [1] = Xu and Kamp, 2000; [2] = Wilson and Fowler, 2011; [3] = Tan et al., 2017a; [4] = Clark et al., 2005; [5] = Tan et al., 2014; [6] = Tian et al., 2015; [7] = Tan et al., 2017b; [8] = Wang et al., 2012; [9] = Ansberque et al., 2018; [10] = Tan et al., 2019; [11] = Tian et al., 2018; [12] = Enkelmann et al., 2006. (b) Drainage divides, major faults, and GPS measurements overlying a map of the depth of the Moho. The Moho depth map is generated by Lu et al. (2019) based on Rayleigh wave tomography of Wei et al. (2017). Blue arrows show GPS measurements with 95% confidence interval in the Eurasian reference (from Liang et al., 2013). (c) Distribution of apatite fission track ages and the samples' elevation along the Y-Y' profile. The location of the Y-Y' profile is shown in Fig. 9a. (d) Topography and crustal structure profile X-X′ across

748 the eastern Tibetan Plateau. Profile location is shown in (a) and largely overlaps the
749 seismic profile of Guo et al. (2013). The precipitation difference is schematically
750 shown as clouds and rains based on the measurements shown in Fig. 3b. Red stars
751 indicate three earthquakes nearby, including, from NW to SE, the 25 Aug 1933 M_s 7.5
752 Diexi, the 18 July 2008 M_s 5.1, and the 13 May 2008 M_s 5.2 events. Yellow dots
753 indicate the aftershocks of the 12 May 2008 M_w 7.9 Wenchuan earthquake.
754 Abbreviations: Pz-Mz sed, Paleozoic-Mesozoic sedimentary rocks; LRQF, Longriqu
755 Fault; MEGF, Maoergai Fault; MJF, Minjiang Fault; WMF, Wenchuan-Maoxian
756 Fault; BYF, Beichuan-Yingxiu Fault; JGF, Jiangyou-Guanxian Fault. Red, grey, and
757 white arrows are not to scale.
758

Table 1. Calculation of the velocity of drainage divide migration in eastern Tibet.

Divide Information		Topographic Parameters Extracted from DEM							Parameters on erosion rate (at least 1 of 4 is required)				Drainage Divide Migration	
Site	Location	Base Elev.	Head Elev.	tanα	tanβ	χ_α/χ_β	k_{sn} (α) ($m^{0.9}$)	k_{sn} (β) ($m^{0.9}$)	E_α (mm/yr)	E_β (mm/yr)	$\bar{E}$ (mm/yr)	K ($10^{-6}m^{0.1}yr^{-1}$)	Direction	Rate (mm/yr)
Min-Jialing drainage divide														
Fig. 5-A	103.819°E, 33.011°N	3500m	3939m	0.47 ± 0.01	0.30 ± 0.01	2.20/5.73	199.55	76.61	0.43 ± 0.14	0.17 ± 0.06	0.30 ± 0.10	2.17 ± 0.72	276°	0.35 ± 0.12
Fig. 5-B	103.834°E, 32.978°N	3500m	4078m	0.33 ± 0.01	0.27 ± 0.01	4.52/5.68	127.88	101.76	0.30 ± 0.08	0.24±0.06 (1)	0.27 ± 0.07	2.36 ± 0.59	231°	0.10 ± 0.06
Fig. 5-C	103.876°E, 32.937°N	3500m	3936m	0.52 ± 0.01	0.26 ± 0.01	3.48/6.39	125.29	68.23	0.44 ± 0.11	0.24±0.06 (1)	0.34 ± 0.09	3.52 ± 0.88	264°	0.26 ± 0.09
Fig. 5-D	103.890°E, 32.890°N	3500m	4093m	0.22 ± 0.01	0.16 ± 0.01	4.84/7.20	122.52	82.36	0.53 ± 0.08 (1)	0.36 ± 0.05	0.44 ± 0.07	4.33 ± 0.65	304°	0.46 ± 0.29
Fig. S6-A	103.869°E, 31.880°N	1700m	2723m	0.38 ± 0.01	0.42 ± 0.01	6.59/8.56	155.24	119.51	0.34 ± 0.11	0.26 ± 0.09	0.30 ± 0.10	2.18 ± 0.73	234°	0.10 ± 0.14
Fig. S6-B	103.907°E, 31.823°N	1700m	2490m	0.67 ± 0.01	0.50 ± 0.01	4.94/7.20	159.92	109.72	0.36 ± 0.12	0.24 ± 0.08	0.30 ± 0.10	2.23 ± 0.74	224°	0.10 ± 0.09
Fig. S7-A	103.821°E, 32.349°N	2600m	3750m	0.61 ± 0.01	0.73 ± 0.01	5.69/7.36	202.11	156.25	0.34 ± 0.11	0.26 ± 0.09	0.30 ± 0.10	1.67 ± 0.56	313°	0.06 ± 0.08
Fig. S7-B	103.803°E, 32.318°N	2600m	4106m	0.69 ± 0.01	0.76 ± 0.01	7.32/8.10	205.74	185.93	0.61 ± 0.08	0.55±0.077 (2)	0.58 ± 0.08	2.96 ± 0.41	261°	0.04 ± 0.08
Fig. S7-C	103.833°E, 32.182°N	2600m	3361m	0.71 ± 0.01	0.66 ± 0.01	4.15/5.28	183.37	144.13	0.34 ± 0.11	0.26 ± 0.09	0.30 ± 0.10	1.83 ± 0.61	263°	0.05 ± 0.08
Fig. S7-D	103.822°E, 32.071°N	2600m	3577m	0.58 ± 0.01	0.54 ± 0.01	5.35/6.88	182.62	142.01	0.72 ± 0.08	0.56±0.065 (2)	0.64 ± 0.07	3.94 ± 0.46	292°	0.14 ± 0.11
Fig. S8-A	103.819°E, 32.816°N	3500m	3920m	0.27 ± 0.01	0.21 ± 0.01	2.61/6.46	160.92	65.02	0.53 ± 0.08 (1)	0.21 ± 0.03	0.37 ± 0.06	3.29 ± 0.50	267°	0.66 ± 0.24
Fig. S8-B	103.738°E, 32.738°N	3500m	3742m	0.24 ± 0.01	0.36 ± 0.01	1.25/2.30	193.60	105.22	0.51 ± 0.05	0.27 ± 0.03	0.39 ± 0.04	2.61 ± 0.26	255°	0.38 ± 0.18
Fig. S8-C	103.883°E, 32.648°N	3500m	4059m	1.00 ± 0.01	0.75 ± 0.01	2.87/3.83	194.77	145.95	0.34 ± 0.11	0.26 ± 0.09	0.30 ± 0.10	1.76 ± 0.59	236°	0.05 ± 0.02
Fig. S8-D	103.786°E, 32.551°N	3500m	3739m	0.60 ± 0.01	0.51 ± 0.01	0.89/1.91	268.54	125.13	0.41 ± 0.14	0.19 ± 0.06	0.30 ± 0.10	1.52 ± 0.51	259°	0.19 ± 0.07
Fig. S9-A	103.418°E, 33.089°N	3500m	3821m	0.37 ± 0.01	0.37 ± 0.01	7.32/8.15	43.85	39.39	0.16 ± 0.02	0.14 ± 0.015 (2)	0.15 ± 0.02	3.55 ± 0.38	189°	0.02 ± 0.02
Fig. S9-B	103.578°E, 33.135°N	3500m	3797m	0.46 ± 0.01	0.40 ± 0.01	3.21/4.90	92.52	60.61	0.36 ± 0.12	0.24 ± 0.08	0.30 ± 0.10	3.92 ± 0.13	232°	0.14 ± 0.06
Fig. S9-C	103.652°E, 33.120°N	3500m	3692m	0.31 ± 0.01	0.39 ± 0.01	2.09/3.62	91.87	53.04	0.38 ± 0.13	0.22 ± 0.07	0.30 ± 0.10	4.14 ± 0.14	210°	0.23 ± 0.09
Dadu-Min drainage divide														
Fig. S2-A	102.977°E, 31.087°N	3700m	4317m	0.96 ± 0.01	0.52 ± 0.01	3.56/7.13	173.31	86.54	0.40 ± 0.13	0.20 ± 0.07	0.30 ± 0.10	2.31 ± 0.77	252°	0.14 ± 0.08
Fig. S2-B	102.901°E, 30.924°N	3700m	4349m	0.67 ± 0.01	0.62 ± 0.01	4.16/6.30	156.01	103.02	0.36 ± 0.12	0.24 ± 0.08	0.30 ± 0.10	2.32 ± 0.77	259°	0.10 ± 0.09
Fig. S3-A	102.687°E, 31.970°N	3500m	4062m	0.34 ± 0.01	0.55 ± 0.01	3.51/4.58	160.11	122.71	0.38 ± 0.05 (2)	0.29 ± 0.04	0.34 ± 0.04	2.37 ± 0.31	255°	0.10 ± 0.12
Fig. S3-B	102.677°E, 31.859°N	3500m	3998m	0.47 ± 0.01	0.33 ± 0.01	3.19/4.11	156.11	121.17	0.34 ± 0.11	0.26 ± 0.09	0.30 ± 0.10	2.16 ± 0.72	311°	0.09 ± 0.13
Fig. S3-C	102.634°E, 31.672°N	3500m	4599m	0.51 ± 0.01	0.79 ± 0.01	6.58/9.45	167.02	116.30	0.35 ± 0.12	0.25 ± 0.08	0.30 ± 0.10	2.12 ± 0.71	283°	0.08 ± 0.08
Fig. S3-D	102.607°E, 31.628°N	3500m	4311m	0.66 ± 0.01	0.54 ± 0.01	4.49/7.05	180.62	115.04	0.37 ± 0.12	0.23 ± 0.08	0.30 ± 0.10	2.03 ± 0.68	284°	0.11 ± 0.09
Fig. S3-E	102.680°E, 31.485°N	3500m	4413m	0.39 ± 0.01	1.08 ± 0.01	5.69/7.61	160.46	119.97	0.34 ± 0.11	0.26 ± 0.09	0.30 ± 0.10	2.14 ± 0.72	274°	0.06 ± 0.07
Fig. S4-A	102.599°E, 32.221°N	3700m	4033m	0.56 ± 0.01	0.34 ± 0.01	3.36/4.06	99.11	82.02	0.33 ± 0.11	0.27 ± 0.09	0.30 ± 0.10	3.31 ± 0.11	278°	0.06 ± 0.12
Fig. S4-B	102.604°E, 32.184°N	3700m	4186m	0.70 ± 0.01	0.40 ± 0.01	3.94/5.57	123.35	87.25	0.42 ± 0.048 (2)	0.30 ± 0.03	0.34 ± 0.04	3.40 ± 0.39	260°	0.11 ± 0.10
Fig. S4-C	102.628°E, 32.124°N	3700m	4227m	0.65 ± 0.01	0.36 ± 0.01	3.92/4.48	134.44	117.63	0.30 ± 0.04 (2)	0.26 ± 0.03	0.34 ± 0.04	2.23 ± 0.30	222°	0.04 ± 0.10
Fig. S5-A	102.714°E, 32.438°N	3950m	4125m	0.46 ± 0.01	0.40 ± 0.01	0.65/2.16	269.23	81.02	0.46 ± 0.15	0.14 ± 0.05	0.30 ± 0.10	1.71 ± 0.57	288°	0.38 ± 0.17
Fig. S5-B	102.674°E, 32.395°N	3950m	4187m	0.19 ± 0.01	0.14 ± 0.01	1.70/3.14	139.41	75.48	0.39 ± 0.13	0.21 ± 0.07	0.30 ± 0.10	2.79 ± 0.93	255°	0.54 ± 0.36

Notes: The uncertainties of migration rates are 1σ. Estimated values for calculation: $\bar{E}$ = 0.30 ± 0.10 mm/yr, ΔU = 0 ± 0.10 mm/yr, K_α/K_β = 1.0 ± 0.1, and n = 1. The underlined numbers in "Parameters on erosion rate" column indicate the input parameters, and others are computed according to each input parameter.

References: (1) Kirkpatrick et al., 2020. (2) Ansberque et al., 2015.

Figure 1

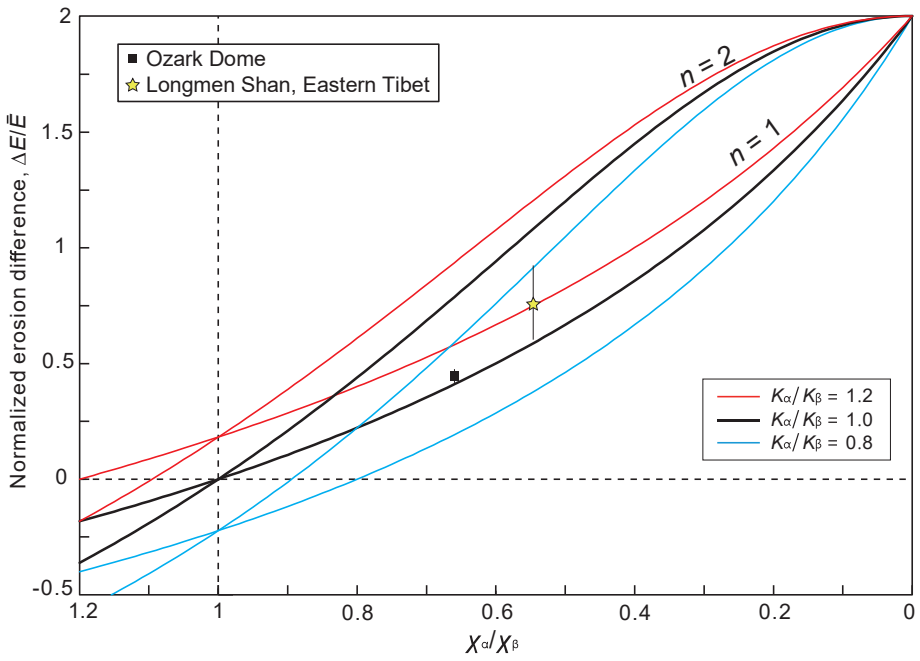
Ozark Dome
Longmen Shan, Eastern Tibet
n = 2
n = 1
Kα/Kβ = 1.2
Kα/Kβ = 1.0
Kα/Kβ = 0.8
Normalized erosion difference, ΔE/Ē
χα/χβ
2
1.5
1
0.5
0
-0.5
1.2
1
0.8
0.6
0.4
0.2
0

Figure 2

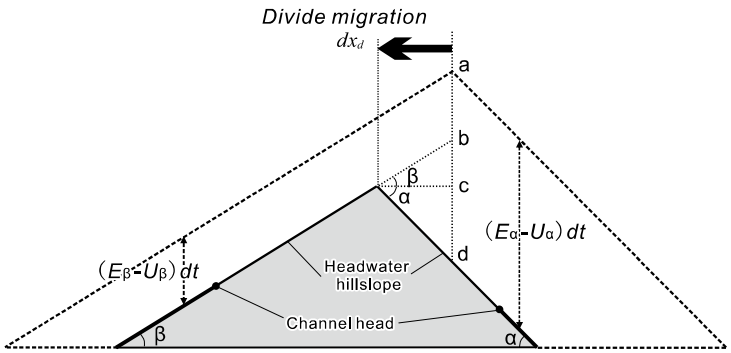
Divide migration
dx_d
a
b
c
d
β
α
$(E_\alpha - U_\alpha)\,dt$
$(E_\beta - U_\beta)\,dt$
Headwater hillslope
Channel head
β
α

Figure 3

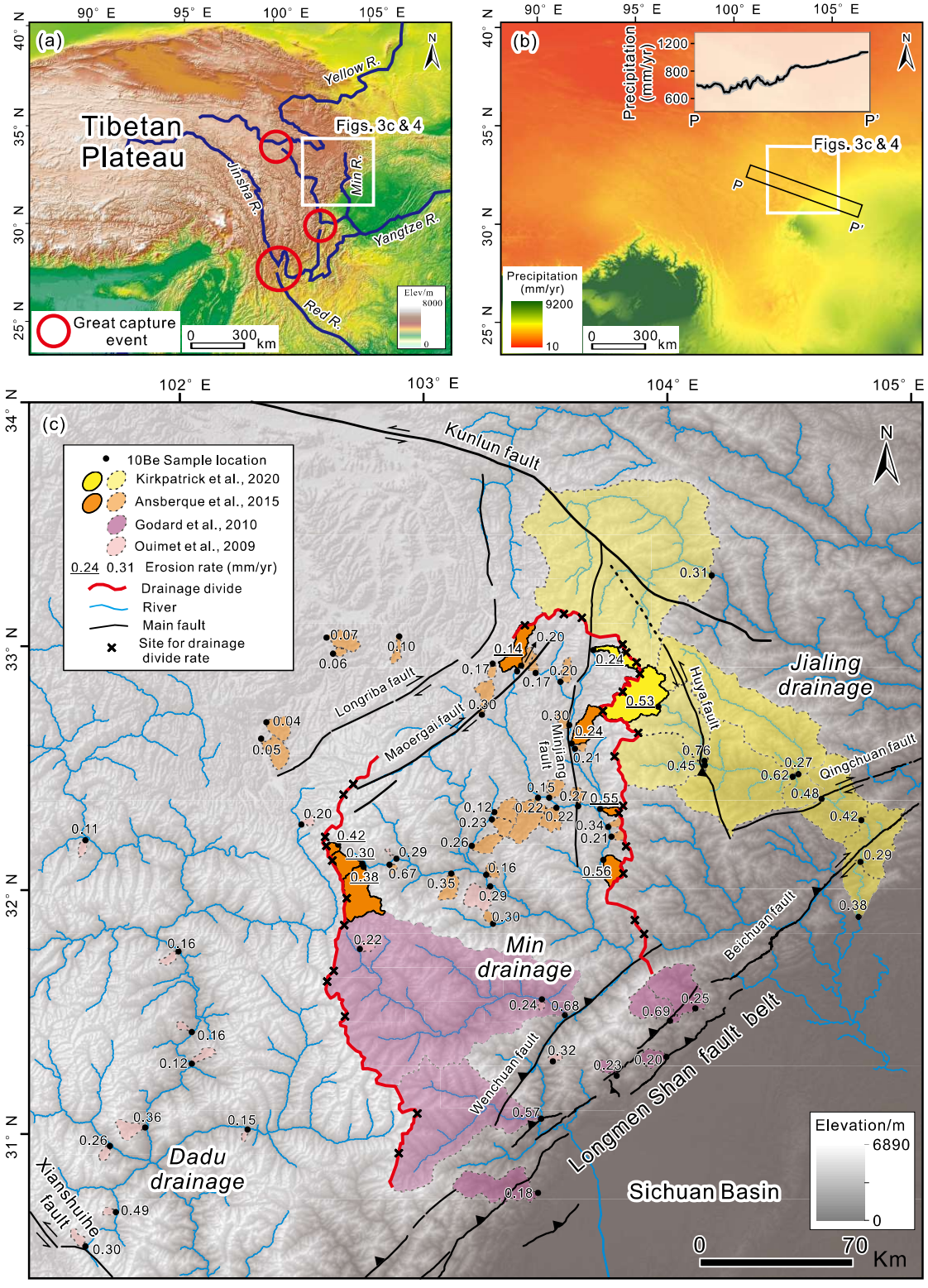
(a)
Tibetan Plateau
Figs. 3c & 4
Yellow R.
Jinsha R.
Min R.
Yangtze R.
Red R.
Great capture event
Elev/m
8000
0
0 300 km
(b)
Precipitation (mm/yr)
1200
800
600
P
P'
Figs. 3c & 4
Precipitation (mm/yr)
9200
10
0 300 km
(c)
10Be Sample location
Kirkpatrick et al., 2020
Ansberque et al., 2015
Godard et al., 2010
Ouimet et al., 2009
0.24 0.31 Erosion rate (mm/yr)
Drainage divide
River
Main fault
Site for drainage divide rate
Kunlun fault
Longriba fault
Maoergai fault
Minjiang fault
Huya fault
Qingchuan fault
Beichuan fault
Wenchuan fault
Longmen Shan fault belt
Xianshuihe fault
Jialing drainage
Min drainage
Dadu drainage
Sichuan Basin
Elevation/m
6890
0
0 70 Km

Figure 4

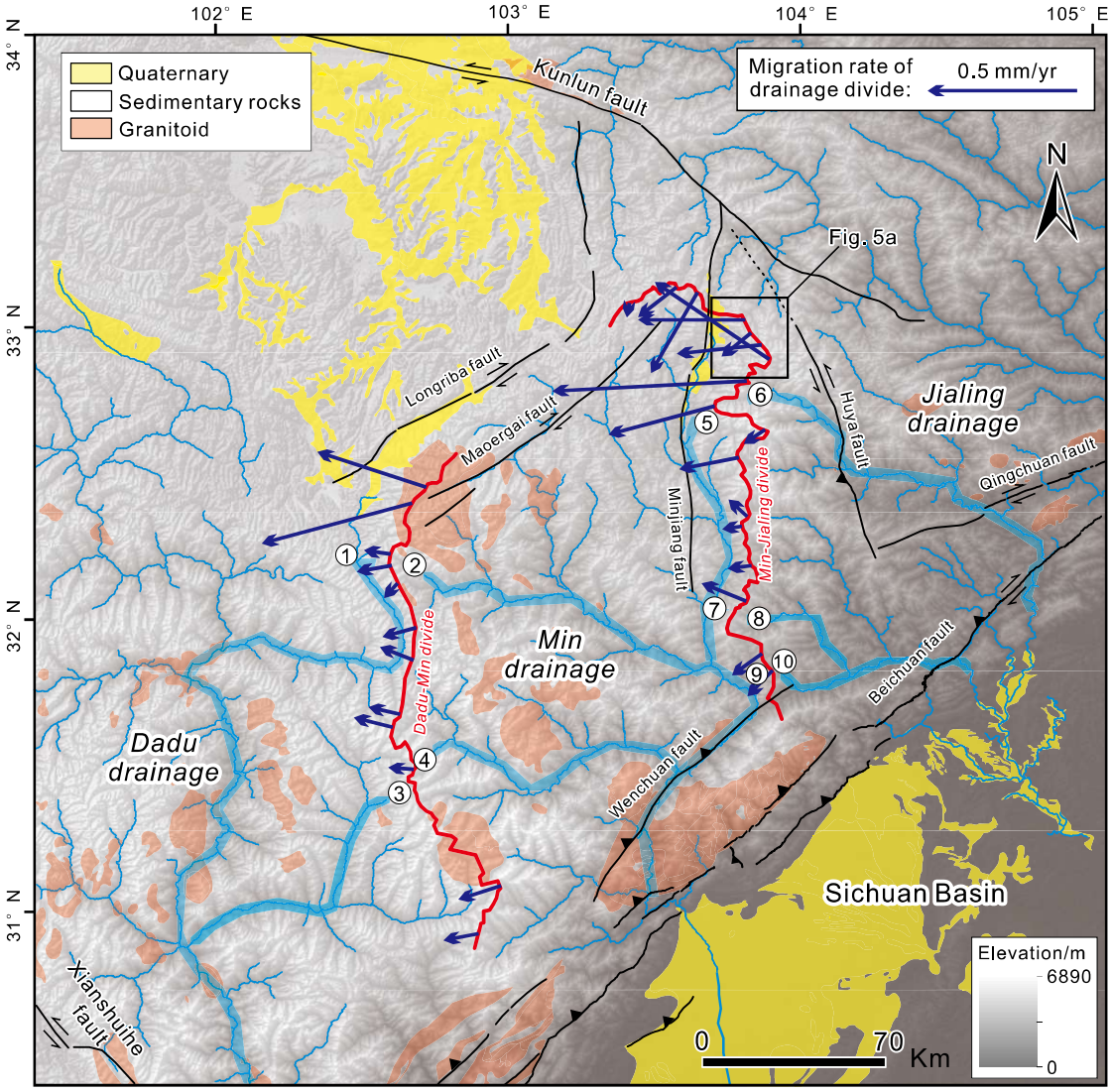
102° E
103° E
104° E
105° E
34° N
33° N
32° N
31° N
Quaternary
Sedimentary rocks
Granitoid
Migration rate of drainage divide:
0.5 mm/yr
N
Fig. 5a
Kunlun fault
Longriba fault
Maoergai fault
Huya fault
Jialing drainage
Qingchuan fault
Minjiang fault
Min-Jialing divide
Dadu-Min divide
Min drainage
Dadu drainage
Beichuan fault
Wenchuan fault
Sichuan Basin
Xianshuihe fault
Elevation/m
6890
0
0
70
Km
1
2
3
4
5
6
7
8
9
10

Figure 5

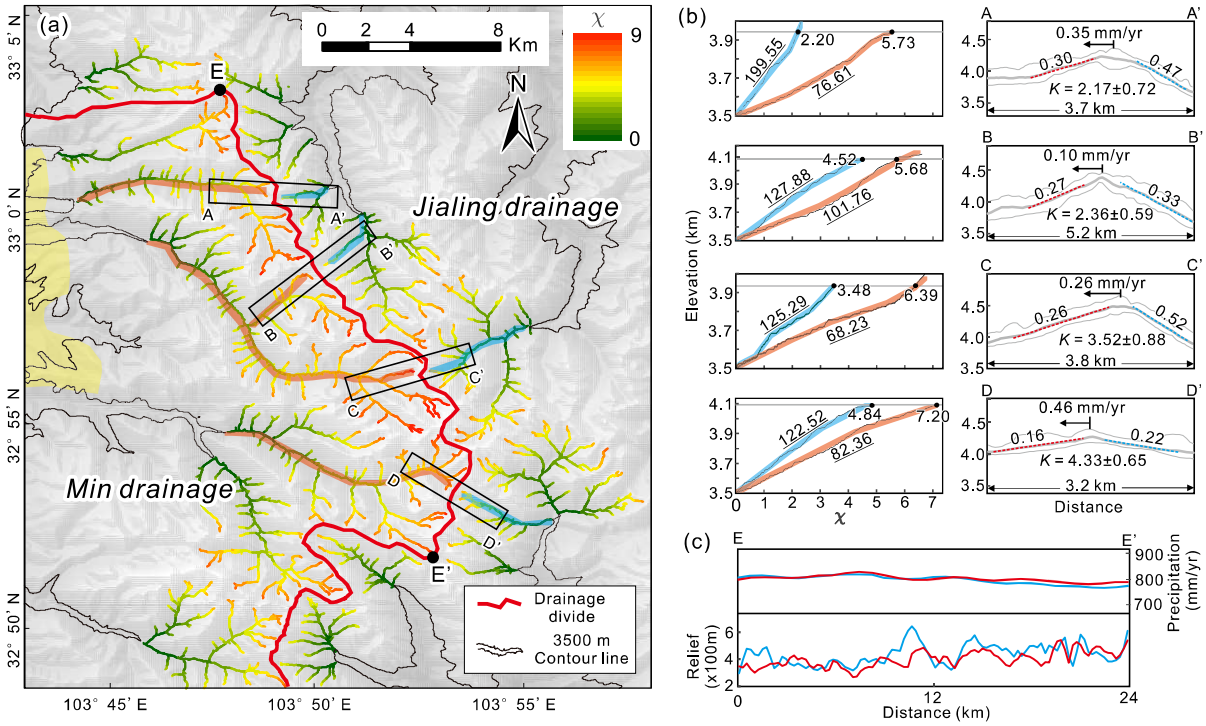
(a)
0 2 4 8 Km
χ
9
0
N
E
E'
A
A'
B
B'
C
C'
D
D'
Jialing drainage
Min drainage
Drainage divide
3500 m Contour line
33° 5' N
33° 0' N
32° 55' N
32° 50' N
103° 45' E
103° 50' E
103° 55' E
(b)
199.55
2.20
5.73
76.61
127.88
4.52
5.68
101.76
125.29
3.48
6.39
68.23
122.52
4.84
7.20
82.36
Elevation (km)
χ
0.35 mm/yr
0.30
0.47
K = 2.17±0.72
3.7 km
0.10 mm/yr
0.27
0.33
K = 2.36±0.59
5.2 km
0.26 mm/yr
0.26
0.52
K = 3.52±0.88
3.8 km
0.46 mm/yr
0.16
0.22
K = 4.33±0.65
3.2 km
Distance
(c)
Relief (x100m)
Precipitation (mm/yr)
Distance (km)

Figure 6

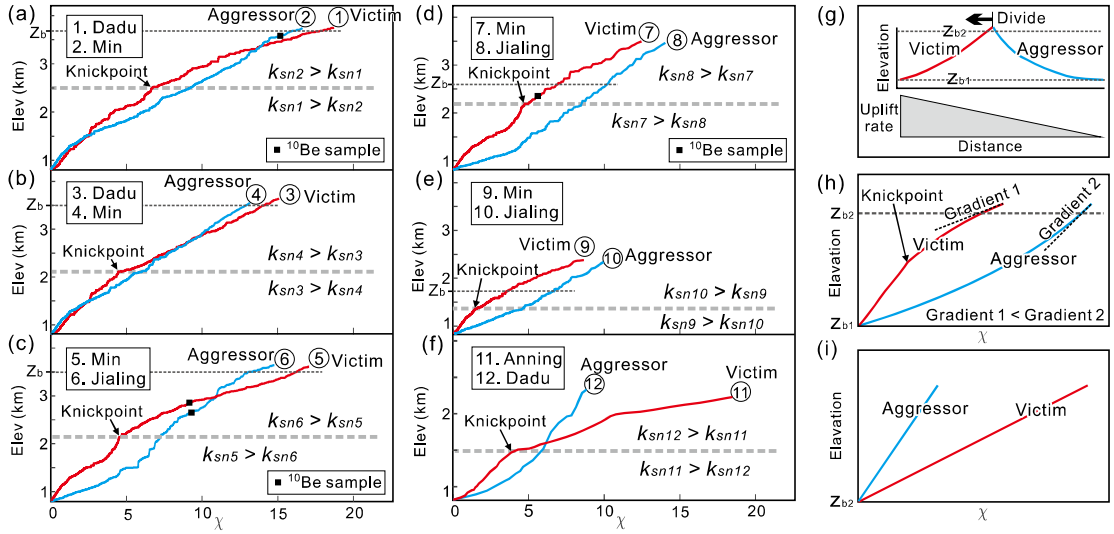
(a)
1. Dadu
2. Min
Aggressor
Victim
Knickpoint
$k_{sn2} > k_{sn1}$
$k_{sn1} > k_{sn2}$
^{10}Be sample
(b)
3. Dadu
4. Min
Aggressor
Victim
Knickpoint
$k_{sn4} > k_{sn3}$
$k_{sn3} > k_{sn4}$
(c)
5. Min
6. Jialing
Aggressor
Victim
Knickpoint
$k_{sn6} > k_{sn5}$
$k_{sn5} > k_{sn6}$
^{10}Be sample
(d)
7. Min
8. Jialing
Victim
Aggressor
Knickpoint
$k_{sn8} > k_{sn7}$
$k_{sn7} > k_{sn8}$
^{10}Be sample
(e)
9. Min
10. Jialing
Victim
Aggressor
Knickpoint
$k_{sn10} > k_{sn9}$
$k_{sn9} > k_{sn10}$
(f)
11. Anning
12. Dadu
Aggressor
Victim
Knickpoint
$k_{sn12} > k_{sn11}$
$k_{sn11} > k_{sn12}$
Elev (km)
χ
(g)
Divide
Elevation
Victim
Aggressor
Uplift rate
Distance
(h)
Knickpoint
Gradient 1
Gradient 2
Victim
Aggressor
Gradient 1 < Gradient 2
(i)
Aggressor
Victim

Figure 7

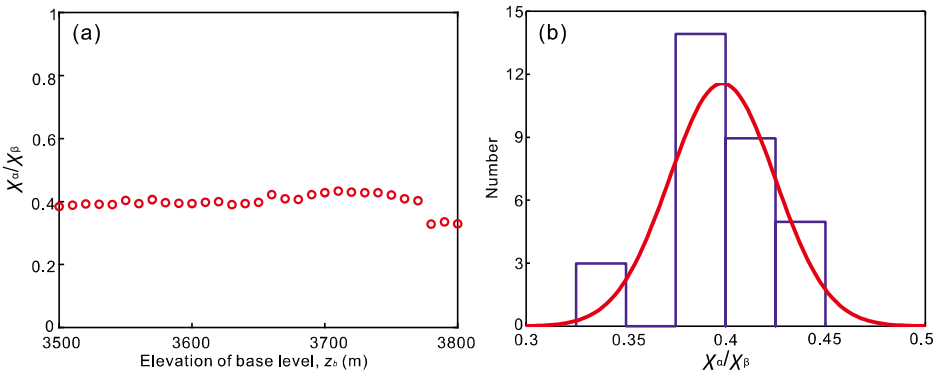
(a)
1
0.8
0.6
0.4
0.2
0
χ_α/χ_β
3500
3600
3700
3800
Elevation of base level, z_b (m)
(b)
15
12
9
6
3
0
Number
0.3
0.35
0.4
0.45
0.5
χ_α/χ_β

Figure 8

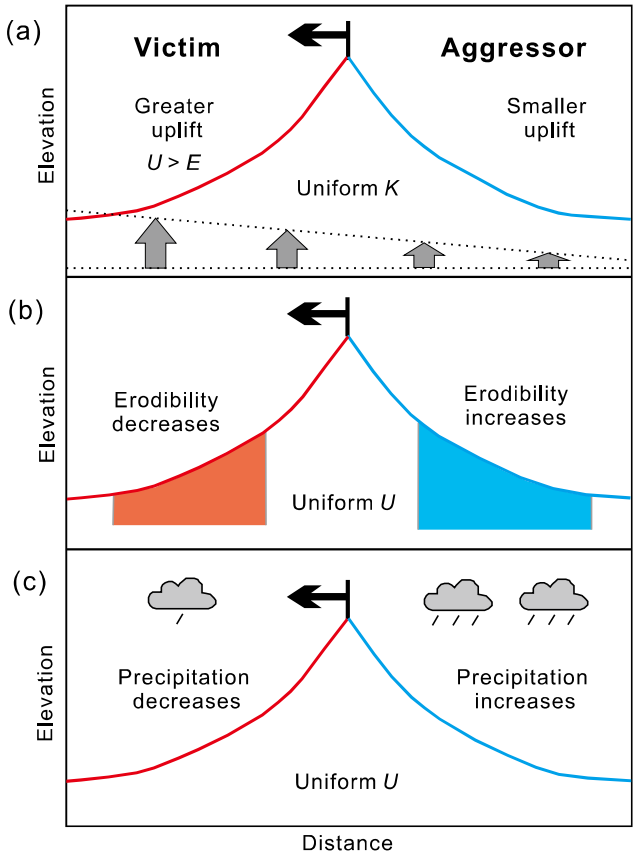
(a)
Victim
Aggressor
Greater uplift
U > E
Smaller uplift
Uniform K
Elevation
(b)
Erodibility decreases
Erodibility increases
Uniform U
Elevation
(c)
Precipitation decreases
Precipitation increases
Uniform U
Elevation
Distance

Figure 9

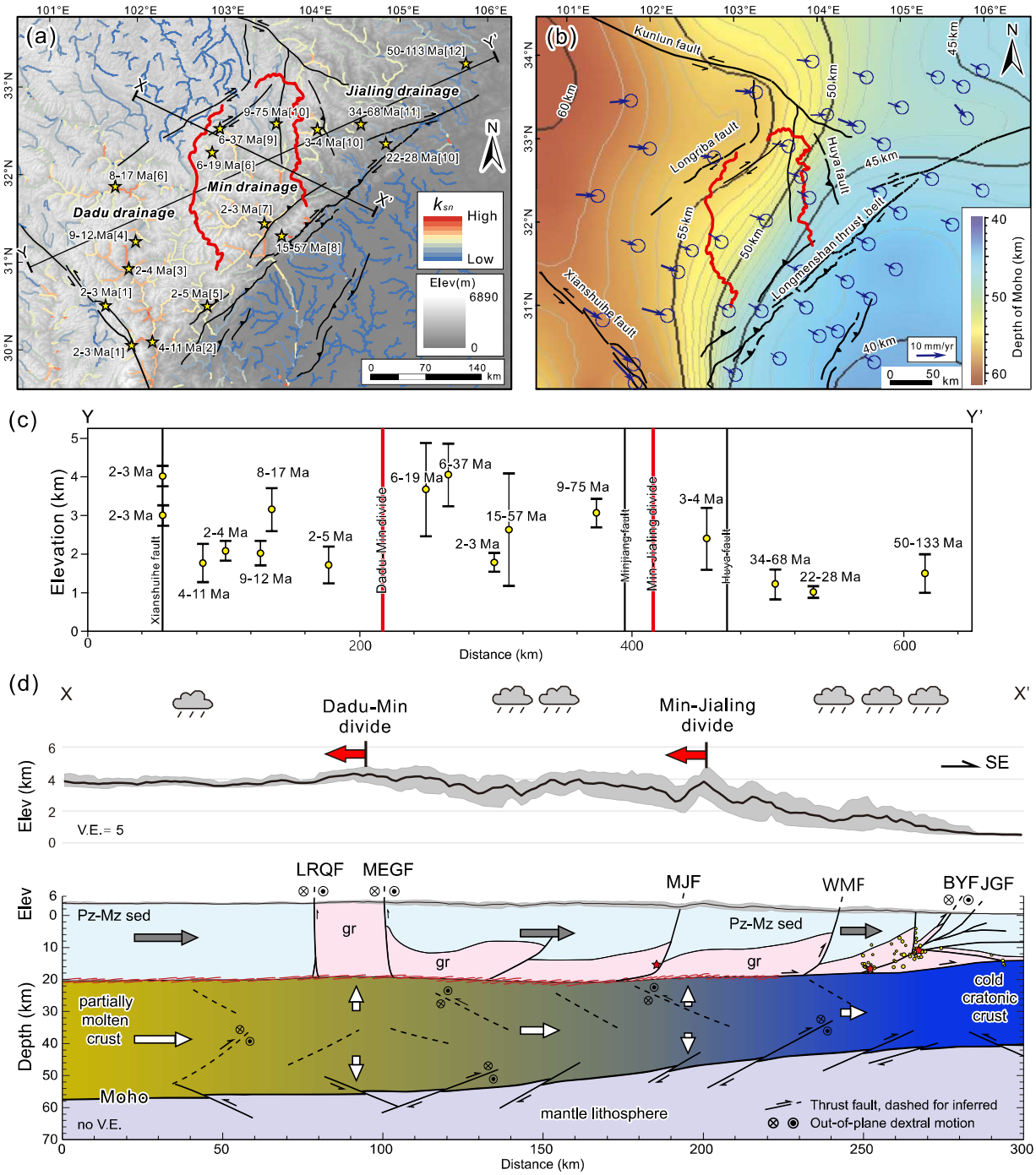
(a)
(b)
(c)
(d)
Jialing drainage
Min drainage
Dadu drainage
50-113 Ma[12]
9-75 Ma[10]
34-68 Ma[11]
6-37 Ma[9]
3-4 Ma[10]
6-19 Ma[6]
22-28 Ma[10]
8-17 Ma[6]
2-3 Ma[7]
9-12 Ma[4]
15-57 Ma[8]
2-4 Ma[3]
2-3 Ma[1]
2-5 Ma[5]
2-3 Ma[1]
4-11 Ma[2]
ksn
High
Low
Elev(m)
6890
0
Kunlun fault
Longriba fault
Xianshuihe fault
Huya fault
Longmenshan thrust belt
60 km
55 km
50 km
45 km
40 km
10 mm/yr
Depth of Moho (km)
Elevation (km)
Distance (km)
Xianshuihe fault
Dadu-Min divide
Minjiang fault
Min-Jialing divide
Huya fault
Dadu-Min divide
Min-Jialing divide
Elev (km)
V.E.= 5
SE
LRQF
MEGF
MJF
WMF
BYF
JGF
Pz-Mz sed
gr
partially molten crust
cold cratonic crust
Moho
no V.E.
mantle lithosphere
Thrust fault, dashed for inferred
Out-of-plane dextral motion
Depth (km)
Distance (km)